



## Prussian Blue Analogues as Positive Electrodes for Mg batteries: Insights into $\text{Mg}^{2+}$ Intercalation

Trocoli, Rafael; Houdeville, Raphaele; Frontera, Carlos; Vincent, Smobin; Lastra, Juan Maria Garcia; Palacin, Rosa

*Published in:*  
ChemSusChem

*Link to article, DOI:*  
[10.1002/cssc.202301224](https://doi.org/10.1002/cssc.202301224)

*Publication date:*  
2024

*Document Version*  
Publisher's PDF, also known as Version of record

[Link back to DTU Orbit](#)

*Citation (APA):*  
Trocoli, R., Houdeville, R., Frontera, C., Vincent, S., Lastra, J. M. G., & Palacin, R. (2024). Prussian Blue Analogues as Positive Electrodes for Mg batteries: Insights into  $\text{Mg}^{2+}$  Intercalation. *ChemSusChem*, 17(5), Article e202301224. <https://doi.org/10.1002/cssc.202301224>

---

### General rights

Copyright and moral rights for the publications made accessible in the public portal are retained by the authors and/or other copyright owners and it is a condition of accessing publications that users recognise and abide by the legal requirements associated with these rights.

- Users may download and print one copy of any publication from the public portal for the purpose of private study or research.
- You may not further distribute the material or use it for any profit-making activity or commercial gain
- You may freely distribute the URL identifying the publication in the public portal

If you believe that this document breaches copyright please contact us providing details, and we will remove access to the work immediately and investigate your claim.

Special  
Collection

# Prussian Blue Analogues as Positive Electrodes for Mg Batteries: Insights into $\text{Mg}^{2+}$ Intercalation

Rafael Trócoli,<sup>[a]</sup> Raphaëlle Houdeville,<sup>[b]</sup> Carlos Frontera,<sup>[b]</sup> Smobin Vincent,<sup>[c]</sup> Juan Maria Garcia Lastra,<sup>[c]</sup> and M. Rosa Palacín<sup>\*[b]</sup>

Potassium manganese hexacyanoferrate has been prepared by co-precipitation from manganese (II) chloride and potassium citrate, with chemical analysis yielding the formula  $\text{K}_{1.72}\text{Mn}[\text{Fe}(\text{CN})_6]_{0.92}\square_{0.08}\cdot 1.1\text{H}_2\text{O}$  (KMnHCF). Its X-ray diffraction pattern is consistent with a monoclinic structure (space group  $P2_1/n$ , no. 14) with cell parameters  $a = 10.1202(6)\text{Å}$ ,  $b = 7.2890(5)\text{Å}$ ,  $c = 7.0193(4)\text{Å}$ , and  $\beta = 89.90(1)^\circ$ . Its redox behavior has been studied in magnesium containing electrolytes. Both  $\text{K}^+$  ions deintercalated from the structure upon oxidation and contamination with  $\text{Na}^+$  ions coming from the separator were found to

interfere in the electrochemical response. In the absence of alkaline ions, pre-oxidized manganese hexacyanoferrate showed reversible magnesium intercalation, and the process has been studied by *operando* synchrotron X-ray diffraction. The location of  $\text{Mg}^{2+}$  ions in the crystal structure was not possible with the available experimental data. Still, density functional theory simulations indicated that the most favorable position for  $\text{Mg}^{2+}$  intercalation is at 32f sites (considering a pseudo cubic  $Fm\bar{3}m$  phase), which are located between 8c and Mn sites.

## Introduction

Today Li-ion batteries are the reference battery chemistry for most applications, from portable electronics to transport electrification and also considered to store energy generated from renewable sources.<sup>[1,2]</sup> Yet, diversification in the technologies is crucial both to reduce dependence of specific raw materials and, most important, to adapt to specific use requirements including not only performance figures of merit (energy density, power, lifetime etc.), but also economic and environmental considerations.<sup>[3,4]</sup>

Among the different possible rechargeable battery concepts, those based on multivalent charge carrier ions, such as  $\text{Mg}^{2+}$ ,  $\text{Ca}^{2+}$ ,  $\text{Zn}^{2+}$  or  $\text{Al}^{3+}$ , have attracted great attention, especially coupled to the use of the corresponding metal as negative electrode. Aside from the case of Zn, which is the most electropositive element that can be plated using aqueous electrolytes, most attention has been placed in Mg based batteries, for which proof-of-concept was achieved already in 2000.<sup>[5]</sup> Mg exhibits high volumetric capacity ( $3833\text{ mAh cm}^{-3}$ ), low standard reduction potential ( $-2.4\text{ V vs. SHE}$ ) and its cost is much lower than that of lithium, as its abundance on the earth crust is significantly higher.<sup>[6,7]</sup> However, Mg batteries have not yet reached the market, as significant hurdles remain, affecting all battery components.

On one side, efficient electroplating with suitable kinetics is crucial, and the electrolyte formulations enabling it developed to date exhibit limited stability at high potential and are mostly corrosive, which severely impacts the cell assembly process.<sup>[8]</sup> On the other, the development of a high-capacity high-voltage positive electrode material able to (de-)intercalate Mg reversibly in the structure is still challenging. Multiple alternatives have been explored, including spinel and layered sulfides or oxides and polyanionic materials, providing often limited capacity or low potential Mg intercalation.<sup>[9–11]</sup> Open framework structures have also recently attracted attention as magnesium insertion hosts. Prussian Blue analogues (PBAs)  $\text{A}_x\text{M}[\text{M}'(\text{CN})_6]_y\cdot z\text{H}_2\text{O}$  ( $\text{A}$  = alkaline metal (mostly  $\text{K}^+$  or  $\text{Na}^+$ );  $\text{M}$  and  $\text{M}'$  = transition metals;  $0 \leq x \leq 2$ ;  $y \leq 1$ ) represent an interesting alternative, which has proved excellent performances in Na and K based batteries, reaching capacities close to the theoretical values and delivering up to 5000 cycles.<sup>[12,13]</sup> The structure of  $\text{A}_x\text{M}[\text{M}'(\text{CN})_6]_y\cdot z\text{H}_2\text{O}$  (Figure 1),<sup>[14]</sup> with  $y = 1$ , consists of a double perovskite framework with  $(\text{C}\equiv\text{N})^-$  anions bridging  $\text{MN}_6$  and  $\text{M}'\text{C}_6$  octahedra;  $\text{A}^+$  and  $\text{H}_2\text{O}$  occupy the cubes defined by the transition metal framework.

[a] Dr. R. Trócoli  
Departamento de Química Inorgánica e Ingeniería Química  
Instituto Químico para la Energía y el Medio Ambiente (IQUEMA), Facultad de Ciencias  
Universidad de Córdoba  
Campus de Rabanales, Córdoba 14071 (Spain)

[b] Dr. R. Houdeville, Dr. C. Frontera, Dr. M. R. Palacín  
Instituto de Ciencia de Materiales de Barcelona (ICMAB-CSIC)  
Campus de la UAB  
08193 Bellaterra, Catalonia (Spain)  
E-mail: rosa.palacin@icmab.es

[c] Dr. S. Vincent, Dr. J. M. Garcia Lastra  
Department of Energy Conversion and Storage  
Technical University of Denmark  
Kongens Lyngby 2800 (Denmark)

Supporting information for this article is available on the WWW under <https://doi.org/10.1002/cssc.202301224>

This publication is part of a joint Special Collection dedicated to Post-Lithium Storage, featuring contributions published in *Advanced Energy Materials*, *Batteries & Supercaps*, and *ChemSusChem*.

© 2023 The Authors. ChemSusChem published by Wiley-VCH GmbH. This is an open access article under the terms of the Creative Commons Attribution Non-Commercial License, which permits use, distribution and reproduction in any medium, provided the original work is properly cited and is not used for commercial purposes.

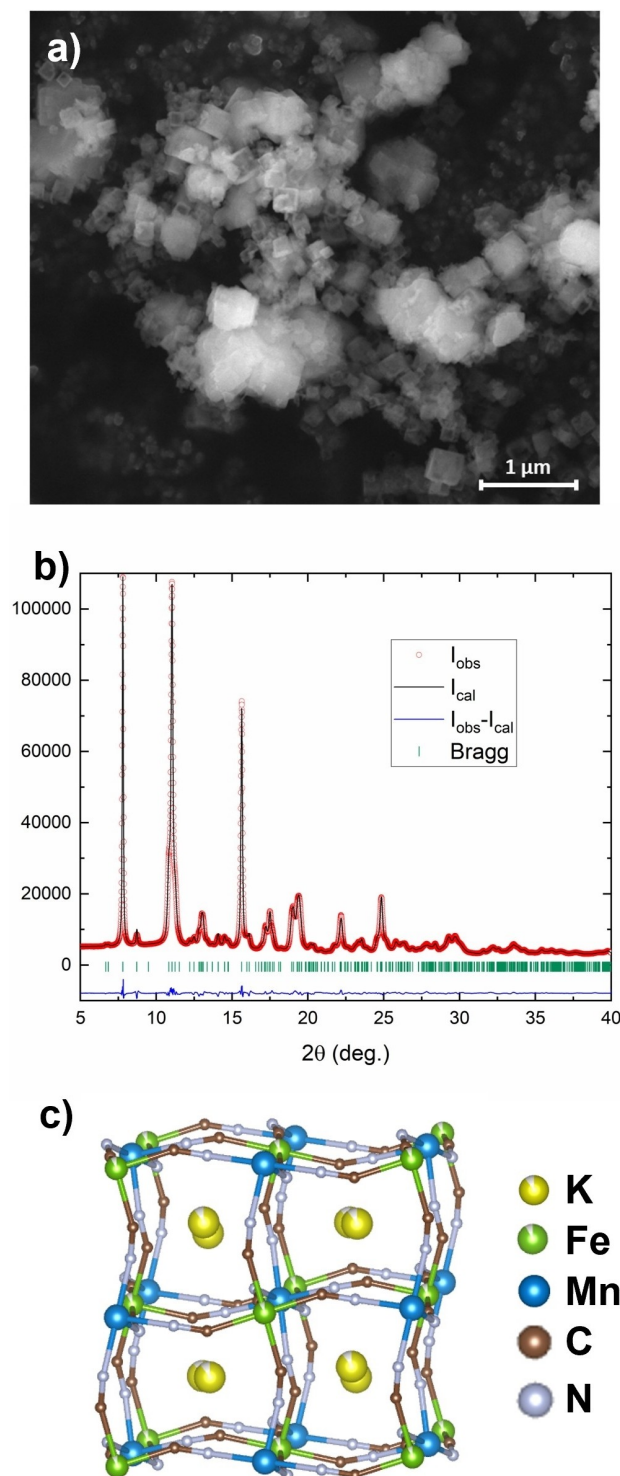


**Figure 1.** A representative SEM image of the as prepared  $K_{1.72}Mn[Fe(CN)_6]_{0.92}\square_{0.08}\cdot 1.1H_2O$  (a) and synchrotron X-ray diffraction (SXR D) pattern with corresponding Rietveld refinement (b). Crystal structure obtained from the Rietveld refinement (c).  $\lambda = 0.6881 \text{ \AA}$ .

These materials have shown the ability to reversibly intercalate multivalent cations in aqueous media ( $Zn^{2+}$ ,  $Cu^{2+}$ ,  $Pb^{2+}$ ,  $Al^{3+}$ ,  $Y^{3+}$ , ...),<sup>[15]</sup> including  $Mg^{2+}$ .<sup>[16]</sup> However, some controversies remain, as recent studies point at the redox response

observed being related to the intercalation of protons rather than divalent ions.<sup>[17]</sup>

The study of these compounds in non-aqueous magnesium-based electrolytes is appealing, if they are ever to be coupled with magnesium metal negative electrodes. A limited number of works have been reported to date. K.-T. Lee *et al.*<sup>[18]</sup> studied the behavior of  $Na_{0.69}Fe_2(CN)_6$  in 0.3 M magnesium bis(trifluoromethane sulfonyl)imide ( $Mg(TFSI)_2$ ) dissolved in acetonitrile (ACN) as electrolyte. The authors report competition between  $Na^+$  and  $Mg^{2+}$  intercalation, which again complicates the interpretation of the redox activity observed. Later on, B. J. Ingram *et al.*<sup>[19]</sup> developed an alternative electrochemical testing protocol to solve the issue.  $NaNi[Fe(CN)_6]$  was fully oxidized to extract  $Na^+$  from the crystal structure and the electrode was then recovered and a new cell assembled with a fresh electrolyte. This new cell would be free from  $Na^+$ , which could reintercalate in the crystal structure and participate in the redox process. The authors proved the intercalation of  $Mg^{2+}$  using  $Mg(TFSI)_2$  in propylene carbonate (PC) as the electrolyte, thanks to a combination of characterization techniques including Energy Dispersive X-ray spectroscopy (EDX), X-ray diffraction (XRD), and X-ray absorption near edge structure (XANES). A significant amount of S on the electrode was detected by EDX, attributed to the decomposition of the TFSI anion, which could also induce the presence of a larger amount of magnesium on the surface. S.-T. Wong *et al.* followed a similar procedure for studying the Mg intercalation in  $K_{1.51}Ni[Fe(CN)_6]_{0.954}\cdot 0.766H_2O$  using 0.5 M  $Mg(ClO_4)_2$  in ACN as electrolyte. Note that in this case, since nickel cannot be oxidized, full extraction of potassium from the crystal structure is not possible. *Ex-situ* XRD on the electrodes reduced in the magnesium based electrolyte indicated minor crystal structure changes concomitant to the reduction up to a capacity consistent with the insertion of 0.27 moles of  $Mg^{2+}$ .<sup>[20]</sup>

In this article, we report a similar study carried out on potassium manganese hexacyanoferrate,  $KMnHCF$ . This compound exhibits higher theoretical capacity ( $\sim 140 \text{ mAh g}^{-1}$ ) than  $ANiHCF$  because of the two active redox centers ( $Mn^{+3}/Mn^{+2}$  and  $Fe^{+3}/Fe^{+2}$ ) that can be involved to compensate the charge related to the  $Mg^{+2}$  insertion process. Once the intercalation of  $Mg^{2+}$  in the crystal structure was established ensuring absence of alkali ions in the electrolyte, the redox mechanism was characterized by *operando* synchrotron X-ray diffraction (SXRD). The changes in the crystal structure were interpreted with the help of theoretical calculations using density functional theory (DFT) simulations which enabled to shed light on the redox mechanism.

## Results and Discussion

The crystal structure of manganese hexacyanoferrate ( $MnHCF$ ,  $M=Mn$ ,  $M'=Fe$ ) has been reported to display different symmetries depending on the synthesis conditions as these affect both the hydration degree and presence of vacancies within the crystal structure. Hydrated monoclinic (space group  $P2_1/n$ ) and cubic ( $Fm-3m$ ) phases have been reported, together with a

completely dehydrated rhombohedral phase (space group  $R\bar{3}$ ).<sup>[14,21]</sup>

The chemical composition of as prepared KMnHCF, calculated considering the results of the analytical techniques described in the experimental section (see also section 1 Sup. Inf.) was found to be  $K_{1.72}Mn[Fe(CN)_6]_{0.92}\square_{0.08}\cdot 1.1H_2O$  (with a rather low amount of vacancies ( $\square$ ), similar than what was found by Wu et al. for the synthesis of NaCoHCF.<sup>[22]</sup> It consists of agglomerates of round-shaped and cubic particles with dimensions ranging from 100 to 350 nm (Figure 1a). Rietveld refinement of its SXRD is consistent with a monoclinic structure (space group  $P2_1/n$ ) indicating a distortion along  $M'-C\equiv N-M$ . (Figure 1b and c). The cell parameters were found to be  $a = 10.1202(6)\text{\AA}$ ,  $b = 7.2890(5)\text{\AA}$ ,  $c = 7.0193(4)\text{\AA}$ , and  $\beta = 89.90(1)^\circ$ . It is worth mentioning that space groups  $P2_1/n$  and  $P2_1/c$  (that used by Pasta and co-workers)<sup>[22]</sup> are equivalent (no. 14), but using a different cell setting (cell parameters found here in  $P2_1/c$  setting are:  $a = 7.0193(4)\text{\AA}$ ,  $b = 7.2890(5)\text{\AA}$ ,  $c = 12.3272(7)\text{\AA}$ , and  $\beta = 124.82(1)^\circ$ ). Contrary to previous reports by J. B. Goodenough et al.<sup>[14]</sup> we were not able to locate the position of oxygen atoms (and by extension, water molecules) since introduction of oxygen did not improve the refinement agreement factors.

Preliminary electrochemical tests were done using  $Mg(ClO_4)_2$  in ACN as electrolyte, KMnHCF exhibited the classic two oxidation peaks in the cyclic voltammetry profile (Figure 2a), which are associated with the oxidation of  $Mn^{2+}$  and  $Fe^{2+}$  and simultaneous  $K^+$  release. A third peak at  $\approx 0.35\text{ V}$  vs. Ag was observed during the reverse scan, which is not reported in classic  $K^+/Na^+$  insertion measurements and could potentially be attributed to  $Mg^{2+}$  intercalation. The energy dispersive X-ray analysis (EDX) of the reduced sample after fourteen galvanostatic cycles (Figure 2b) showed minimal Mg presence (Mg/Mn and K/Mn atomic ratios equal to 0.2 and 1.7 respectively), which might indicate that the electrochemical response was related mainly to the intercalation of  $K^+$  instead of  $Mg^{2+}$  (see section 2 Supporting Information).

In order to elucidate whether the charge compensation mechanism could involve reintercalation of  $K^+$  ions present in the electrolyte after oxidation (estimated K concentration  $\approx 10\text{ mM}$  compared to  $100\text{ mM Mg}$ ), the testing protocol was adapted, not only following the method by Ingram *et al.*<sup>[19]</sup> but also optimizing the separator choice to ensure that no alkali ion contamination could take place (see section 2 in the Supporting Information). In this configuration KMnHCF was first oxidized with low current density (Figure S2) in order to extract the maximum possible amount of  $K^+$ . These oxidized samples are denoted MnHCF throughout the text. After the oxidation step, cells were opened, and the working electrodes washed with dimethyl carbonate and a new cell assembled using fresh electrolyte and a new separator. Galvanostatic reduction in the new cell yields a profile consisting of a pseudo-plateau, reaching up to *ca.*  $95\text{ mAhg}^{-1}$  in capacity (Figure S4), which could be attributed exclusively to  $Mg^{2+}$  intercalation since EDX analysis indicated an increase in the magnesium content with alkali metal impurities being negligible (Mg/Mn and Na/Mn ratios 0.65 and 0.02 respectively). It is worth highlighting that chlorine

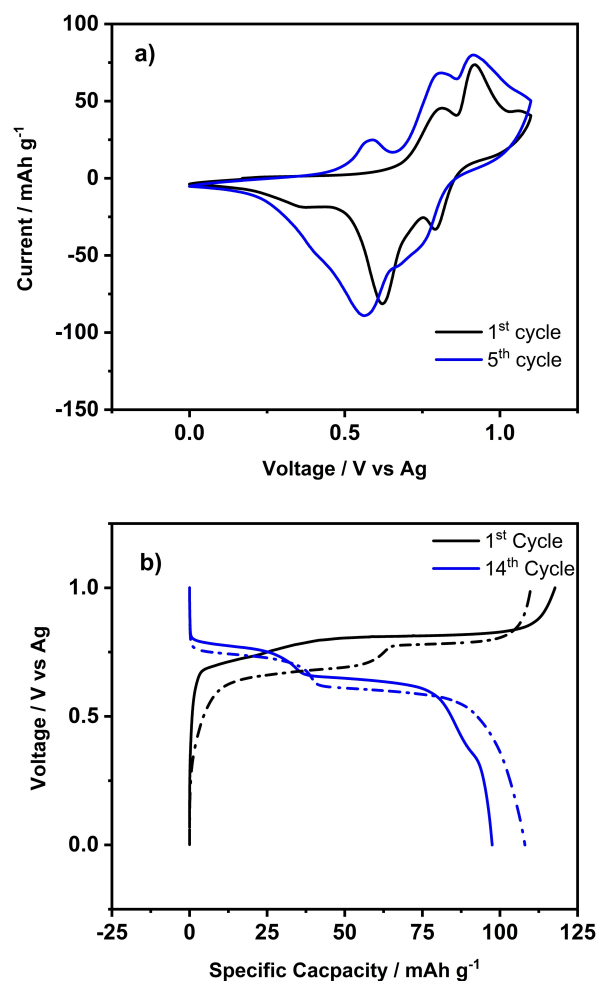


**Figure 2.** Cyclic voltammetry (a) and galvanostatic cycling (b) of  $K_{1.72}Mn[Fe(CN)_6]_{0.92}\square_{0.08}\cdot 1.1H_2O$  in  $0.1\text{ Mg(ClO}_4)_2$  in ACN as electrolyte.

was not detected, which is in agreement with absence of electrolyte adsorption and hence insertion of  $Mg^{2+}$  ions in the crystal structure being the source of the increase in magnesium content.

The redox mechanism was further studied by *operando* SXRD coin cells with a window suitable for *in situ* studies. These were assembled as described in the experimental part with either pristine KMnHCF or an electrochemically pre-oxidized sample (MnHCF) as working electrode and tested using  $0.5\text{ MMg(TFSI)}_2$  in PC as electrolyte and cellulose separator. In order to further assess both the interference of  $K^+$  present in the electrolyte, and the structural changes related to the intercalation of  $Mg^{2+}$  a comparative study was carried out: one cell was assembled with as prepared KMnHCF as working electrode (in which  $K^+$  would be released to the electrolyte during first oxidation and remains for the subsequent reduction step, equivalent to the case depicted in Figure 2), and the other assembled with fresh electrolyte and MnHCF, where no  $K^+$  impurities should be present. An additional control experiment was also performed with as prepared KMnHCF in  $0.5\text{ M KTFSI}$  in PC as electrolyte, which yielded, as expected, results consistent with previous studies in a different electrolyte (Figure S5).<sup>[23]</sup>



The electrochemical profiles of the two *operando* experiments: the cell cycled with pristine KMnHCF, in which  $K^+$  would be present in the electrolyte and the one carried out with a pre-oxidized working electrode (MnHCF) and fresh electrolyte are depicted in Figures 3a) and 3b) respectively. The electrochemical profiles for the first oxidation are rather similar with two consecutive pseudo-plateaus up to 1.5 V (vs AC counter electrode) and slightly additional capacity achieved in the oxidation of MnHCF at the end of oxidation at high voltage.

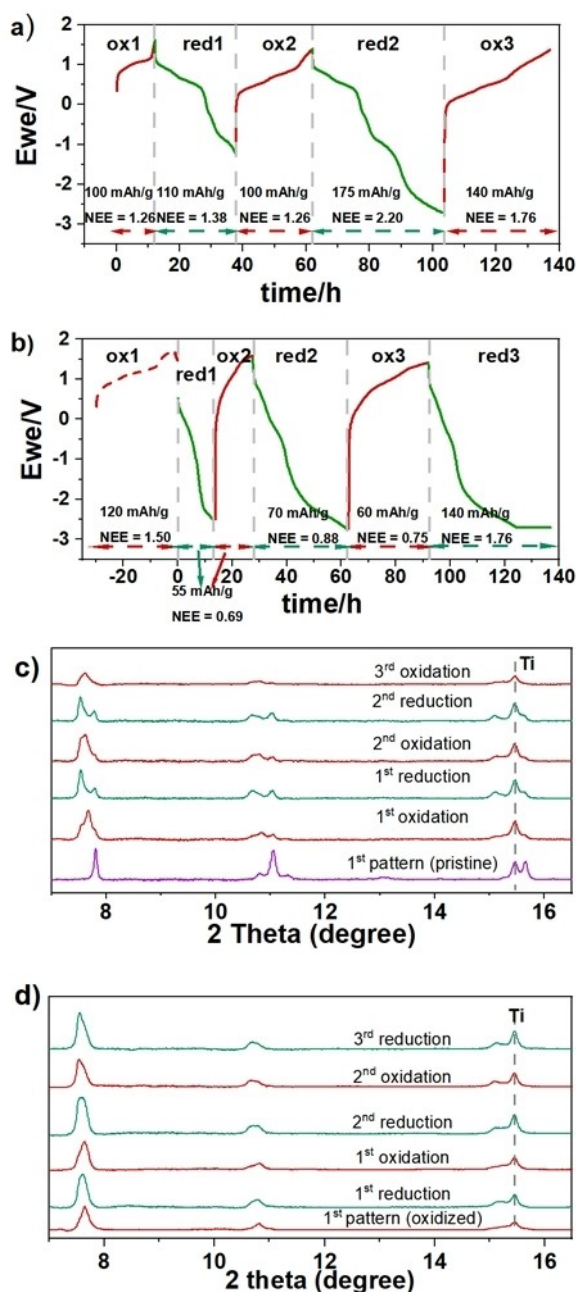


**Figure 3.** Electrochemical profiles of the *operando* experiments with either KMnHCF(a)) or MnHCF (b) as working electrodes with capacities in each step reported both in mAh/g and number of exchanged electrons per formula unit (NEE). The *ex situ* preoxidation profile to obtain MnHCF is presented as a dotted electrochemical curve. Selected patterns at the end of each redox step are shown for KMnHCF (c) and MnHCF (d).

Yet, significant differences can be seen for the first reduction and second oxidation, with the profile of KMnHCF being similar to what is observed when using KTFSI as electrolyte and that of MnHCF showing significantly lower capacity and high polarization, which would be in agreement with more sluggish transport of divalent ions. Normalized patterns (with background correction) measured at the end of each reduction/oxidation step in the  $2\theta$  region  $7\text{--}16.5^\circ$  where the changes are the most visible are shown in Figures 3c) and 3d) for KMnHCF and MnHCF respectively.

The patterns at the end of the first oxidation are slightly different due to some little amount of unreacted pristine phase in the case of KMnHCF, which is consistent with the somewhat smaller capacity achieved, as mentioned above. For better visibility of the subtle changes taking place along each redox step and also to better grasp the different evolution between the two cells, difference patterns with a subtraction of the first pattern of each step were also plotted in 3D (Figures S6 and S8 for KMnHCF and MnHCF respectively). In this representation, a positive intensity is correlated to peak appearance in the course of the process while negative values indicate the opposite, both with respect to the first pattern of the step. A more detailed description of the changes observed in KMnHCF is included in section 4 of the Supporting Information but in summary, the results are in full agreement with the redox mechanism involving two successive two-phase steps (see also Figure S7), as described by Komaba and co-workers in cells containing a potassium electrolyte.<sup>[23]</sup> These results point at the charge compensation mechanism for the redox activity of the transition metals being to a large extent related to  $K^+$  extraction/insertion, which is in agreement with the *ex situ* EDX results mentioned above (Figure 2 and section 2 Supporting Information), with minor intercalation of  $Mg^{2+}$ .

The analogous *operando* experiment carried out with a pre-oxidized working electrode (MnHCF) and fresh electrolyte yielded somewhat different results (see Table S2 in the SI for the details of the changes in peak positions (and corresponding d values) observed for *operando* experiments involving both KMnHCF and MnHCF)). The first pattern collected for MnHCF presents peaks centered at  $7.64^\circ$  and  $10.81^\circ$  (corresponding to  $5.16\text{ \AA}$  and  $3.65\text{ \AA}$  in terms of d-spacing, respectively, Figure 3d) which could be related to the presence of a fully oxidized tetragonal phase, although the width of the peaks might indicate remains of the monoclinic and cubic phases. A first reduction was carried out at C/25 down to  $-2.5\text{ V}$  (vs AC counter electrode). In the early stages of reduction ( $<30\text{ mAh/g}$ ), these peaks slightly shift towards lower angles ( $2\theta = 7.61^\circ$  ( $d = 5.18\text{ \AA}$ ) and  $10.76^\circ$  ( $d = 3.67\text{ \AA}$ )). The 3D difference plots (Figure 4a)), indicate loss of intensity at  $7.65^\circ$  ( $d = 5.15\text{ \AA}$ ) and  $10.81^\circ$  ( $d = 3.65\text{ \AA}$ ) which is consistent with the disappearance of the tetragonal phase to the expense of a new set of peaks at  $7.55^\circ$  and  $10.68^\circ$  (d-spacing of  $5.22\text{ \AA}$  and  $3.7\text{ \AA}$  respectively) which do not seem to correspond to any of the phases observed in previous experiments where  $K^+$  insertion took place and hence might be related to the intercalation of  $Mg^{2+}$  in the crystal structure. Upon further reduction, the changes are minimal, with only a slight increase in the intensities of these

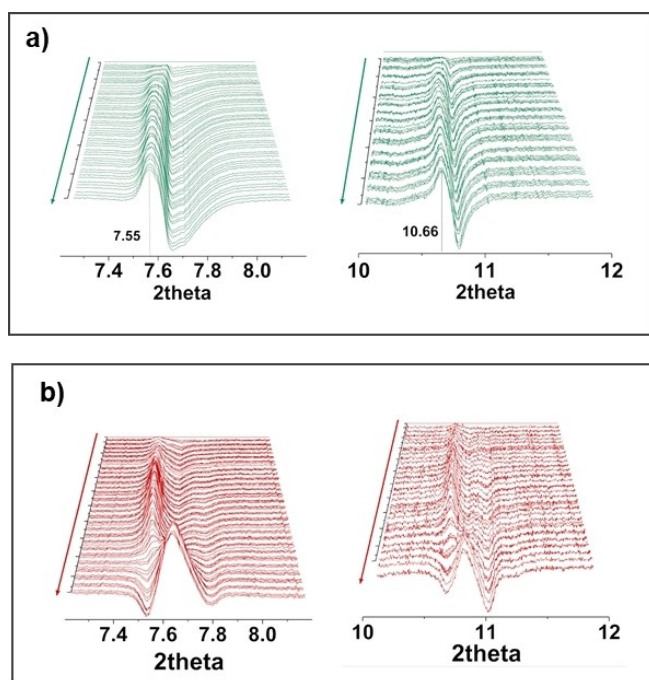


**Figure 4.** 3D difference plots for patterns collected during first reduction (green) (a) and second oxidation (red) (b) of MnHCF *operando* diffraction experiment, with a subtraction of the first pattern of the step.

peaks. Ultimately, this first reduction reaches a capacity of 55 mAh/g which is lower than the one observed when  $K^+$  ions were present in the electrolyte (see Figures 3a and 3b). Further oxidation was carried out at C/25 up to 1.6 V (vs AC counter electrode). On the first stages of the process (< 35 mAh/g), the peaks from the phase seem to widen and shift towards lower angles and intensity loss can be observed at  $7.62^\circ$  and  $10.76^\circ$  (d-spacing = 5.03 Å and 3.56 Å) in the 3D difference plots (Figure 4b)) to the expense of appearance of new peaks at  $7.50^\circ$  and  $10.62^\circ$  (d-spacing = 5.11 Å and 3.61 Å). The changes observed upon oxidation were in agreement with the evolution reported by Komaba,<sup>[23]</sup> with the formation of a new intermediate phase. Upon extended oxidation (> 35 mAh/g), the intensity of the peaks related to this intermediate phase decreases, and in the subtracted pattern (Figure 4b) a negative intensity is detected at  $2\theta = 7.55^\circ$  and  $10.68^\circ$  (phase formed upon reduction and presumably containing magnesium), while a new set of peaks grow in intensity, with main peaks at  $7.7^\circ$  and  $10.85^\circ$  (d-spacing = 4.98 Å and 3.53 Å) which could correspond to the tetragonal oxidized phase, again in agreement with known structural evolution upon oxidation despite somewhat smaller cell parameters. A second reduction was carried out at C/50 which reached a capacity of 70 mAh/g (Figure 3b). Similarly to the first reduction, the peaks at  $7.67^\circ$  and  $10.82^\circ$  lose intensity to the expense of contributions at  $7.53^\circ$  and  $10.67^\circ$  (see Figure S8), which would be in agreement with the conversion of the tetragonal fully oxidized phase to a new Mg-inserted phase. In the stacked patterns (Figure 3d), this transformation is evidenced by a broad peak between  $7.53^\circ$  and  $7.63^\circ$  (corresponding to 5.23 Å and 5.17 Å) and  $10.63^\circ$  and  $10.80^\circ$

(corresponding to 3.71 Å and 3.65 Å). Upon third oxidation at C/50 (Figure 3b), (slower cycling than previous oxidations to analyze the potential influence of the current rate) a shift of the peaks towards lower angles is observed ( $7.54^\circ$  and  $10.65^\circ$  (5.23 Å and 3.70 Å)). The 3D difference plots (Figure S8) indicate that only the new intermediate phase was formed despite the capacity was similar to the capacity in reduction (60 mAh/g) and the tetragonal phase, typically obtained when the oxidation is completed, was not reached. A last (third) reduction was performed down to  $-2.8$  V (vs AC counter electrode), with 80 mAh/g total capacity (Figure 3b) and during which the changes on the XRD patterns are similar to that of the second reduction step described earlier. The cell was kept at  $-2.7$  V vs AC for 15 hours, but no further changes were observed in the patterns.

The above-mentioned results seem to imply the intercalation/deintercalation of  $Mg^{2+}$  ions in the crystal structure taking place in absence of  $K^+/Na^+$  ions in the electrolyte, which is in agreement with the fact that the Mg/Mn ratio deduced from EDX in the working electrode of the K/Na-free cell retrieved after the last reduction step was six times higher than the K/Mn ratio (Section 2 Supporting Information). The changes observed upon intercalation of  $Mg^{2+}$  are subtler than those observed when  $K^+$  is inserted, which is due on one hand to the lower observed capacity, and to the other, to the fact that given the difference in the charge of both ions, even if the same capacity was achieved the amount of  $Mg^{2+}$  ions inserted in the crystal structure would be half of that of  $K^+$ .

Since the available data, consisting of mixtures of phases with very similar cell parameters and significant peak width did preclude attempts to refine the magnesium content in the crystal structure, simulated SXRD patterns were calculated placing different amounts of  $K^+$  and  $Mg^{2+}$  in the structure to try to at least elucidate trends (see section 6 Supporting Information). The cubic intermediate phase described by Komaba<sup>[23]</sup> was chosen for such purpose. Simulations were carried out considering theoretical capacity and considering different possible position for Mg: 8c (center of the cubes), 24d (center of the face) and several positions on the diagonal between the Fe and Mn atom named 32f (positions between Fe and the center were named 32f1 and between the center and Mn atom were named 32f2 – see Figure 5). The results are displayed in Figure S9. Unfortunately, the difference between each simulated pattern is subtle, the relative intensity of the peaks change slightly, and only a peak with very low intensity appears at  $6.53^\circ$  (6.03 Å in d-spacing) in some cases (32f2b and 32f2b).

First-principle calculations based on DFT were performed to elucidate the preferred Mg intercalation site in the structure. Three different magnesium contents were considered, namely  $Mg_{0.25}FeMn(CN)_6$  (i.e., 1 Mg per unit cell),  $Mg_{0.5}FeMn(CN)_6$  (i.e., 2 Mg per unit cell), and  $MgFeMn(CN)_6$  (i.e., 4 Mg per unit cell). For each case, the relative energies of the 8c, 24d, 32f1, and 32f2 Mg intercalation sites (Wyckoff positions corresponding to a pseudocubic  $Fm\bar{3}m$  unit cell,  $Z=4$ ) were computed. In the case of  $Mg_{0.5}FeMn(CN)_6$ , the two inserted Mg ions were placed in opposite cubes within the unit cell to minimize their

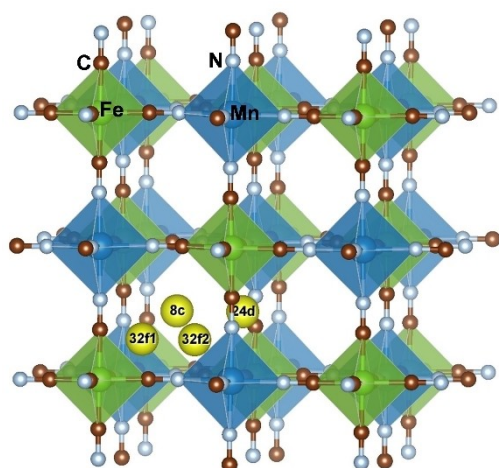


**Figure 5.** Crystal structure of cubic Prussian blue analogue with different possible positions for Mg intercalation: 8c (centre of cube), 24d (centre of face), 32f1 (between centre of cube and Fe atom), and 32f2 (between centre of cube and Mn atom). Fe (Light green), Mn (Dark blue), C (Dark brown), N (Grey), Possible Mg positions (Yellow).

electrostatic repulsion, being both Mg at the same type of site (i.e., either two Mg in two 8c sites, two Mg in two 24d sites, two Mg in two 32f1 sites, or two Mg in 32f2 sites). A similar procedure to minimize the electrostatic repulsion was followed for  $\text{MgMnFe}(\text{CN})_6$ . At this point, it is important to remark that the DFT simulations allowed the relaxation of the unit cell dimensions and symmetry. Although the structures were initialized in cubic crystal systems, most of them underwent crystal symmetry reductions (see Table 1). For the sake of consistency, even though the crystal symmetry was reduced, the site nomenclature of the cubic crystal system was kept for all the cases.

For all magnesium contents, site 32f2 (the one between the center of the cubes and the Mn sites) was found to be the preferred one for Mg intercalation. Table 1 gathers the energy per inserted Mg at each specific site relative to the energy per inserted Mg at the 32f2 sites. It was not possible to obtain results for the 8c sites, because the simulations initialized with Mg ions at this site spontaneously evolved towards the configuration in which Mg ions intercalate at the 32f2/24d sites. This indicates that 8c sites are rather unstable for Mg intercalation. The second most stable site for Mg intercalation is the 24d, which is around 0.6 eV above the 32f2 site energy. This

difference represents a lower bound for the Mg diffusion barrier energy, since Mg percolation would involve Mg displacement from a 32f2 site in a cube to another 32f site in an adjacent cube, which unavoidably must happen through a cube face (i.e., nearby to a 24d site).

## Conclusions

The reversible intercalation of  $\text{Mg}^{2+}$  in pre-oxidized Prussian Blue Analogue,  $\text{MnHCF}$ , has been proved by postmortem EDX and in-situ SXRD measurements. Pre-oxidation of  $\text{KMnHCF}$  at low current densities and use of a fresh electrolyte together with a cellulose-based separator were required to avoid  $\text{K}^+/\text{Na}^+$  contamination, which seem to preferentially intercalate in  $\text{MnHCF}$  instead of  $\text{Mg}^{2+}$  even if present in much lower amount. A different electrochemical profile is observed in absence of alkaline ions, with higher polarizations and lower capacities being achieved upon  $\text{Mg}^{2+}$  insertion. The process was followed by *operando* SXRD. The experiment using pristine  $\text{KMnHCF}$  as electrode active material revealed the well-known electrochemical behavior (two plateaus, capacities around  $120 \text{ mAh g}^{-1}$ ), in agreement with the presence of  $\text{K}^+$  in the electrolyte and the successive two-phase steps involving the transformation from monoclinic to cubic and then tetragonal phases. In contrast,  $\text{MnHCF}$  exhibits a different mechanism with somewhat sluggish transformations and the formation of different phases. Since the location of the intercalated  $\text{Mg}^{2+}$  in the crystal structure was not possible from the data achieved, DFT simulations suggested that the most favorable position for  $\text{Mg}^{2+}$  intercalation is at 32f sites, which are located between the center of the cubes and Mn sites.

## Experimental

$\text{K}_{1.72}\text{Mn}[\text{Fe}(\text{CN})_6]_{0.92}\square_{0.08}\cdot 1.1\text{H}_2\text{O}$  was obtained by a precipitation method in aqueous media using a protocol similar to the one described by Wu *et al.*<sup>[24]</sup> The process is based on the simultaneous dropwise addition at  $0.5 \text{ mL/min}$  flow of two precursor solutions (50 ml of distilled water) under constant vigorous stirring. A mixture of 5 mmol of  $\text{MnCl}_2\cdot 4\text{H}_2\text{O}$  (Sigma Aldrich) and 5 mmol of potassium citrate ( $\text{KH}_2\text{C}_6\text{H}_5\text{O}_7\cdot 3\text{H}_2\text{O}$ ) in 50 ml of distilled water forms solution A, while Solution B contains 5 mmol of  $\text{K}_4\text{Fe}(\text{CN})_6$  in 50 mL of distilled water. The resulting solution was kept under stirring for 12 h and then left for sedimentation of the precipitated particles another 12 h. The supernatant was removed with a Pasteur pipet

**Table 1.** Intercalation energy per Mg atom (in eV) at 24d, 32f1, and 32f2 sites relative to the intercalation energy per Mg atom at the 32f2 site (set as the zero energy) for different magnesium contents. The crystal symmetry structure is also shown.

		24d	32f1	32f2
$\text{Mg}_{0.25}\text{MnFe}(\text{CN})_6$	Energy	0.57	2.09	0
	System	Quasi-tetragonal	Quasi-tetragonal	Quasi-tetragonal
$\text{Mg}_{0.5}\text{MnFe}(\text{CN})_6$	Energy	0.63	0.47	0
	System	Tetragonal	Monoclinic	Monoclinic
$\text{MgMnFe}(\text{CN})_6$	Energy	1.19	2.5	0
	System	Monoclinic	Rhombohedral	Monoclinic



and the precipitate was recovered by centrifugation at 30,000 rpm for 15 min. The product was washed three times with distilled water and once with ethanol, and dried overnight at 70 °C.

Chemical analysis was performed by UAB's Servei d'Anàlisi Química. The metal content was deduced from Inductively Coupled Plasma Optical Emission spectroscopy measurements (ICP-OES, Agilent, model 5900) on a solution prepared with HNO<sub>3</sub> 1 % (v/v) for sample digestion in a microwave. Carbon and Nitrogen amounts were quantified by gas chromatography (Elemental Analysis CHNS Thermo Scientific Flash 2000) after combustion of the samples at 1200 °C in oxygen atmosphere.

Scanning Electron Microscopy images (SEM) and Energy Dispersive X-ray analysis (EDX) were carried out with a Quanta 200 ESEM FEG from FEI. Images were typically collected at 15 keV under  $6.43 \times 10^{-4}$  Pa vacuum.

Thermogravimetric analysis (TGA) were obtained using a Perkin Elmer DSC85000. Samples were heated under nitrogen flow at a rate of 10 °C/min up to 500 °C.

Synchrotron XRD patterns were collected on ALBA-CELLS BL04-MSPD beamline<sup>[25,26]</sup> at  $\lambda = 0.6881$  Å (18 keV). For *operando* experiments, glass window CR2032 coin cells were used, mounted on a multi-cell sample holder as described by Herklotz<sup>[27]</sup> which enabled sequential data collection so that patterns were collected in each cell every 15 minutes. The same separator, counter/reference electrode, electrolyte, and cycling conditions as for the below described standard coin cells were used.

Electrodes were prepared by mixing KMnHCF, carbon black (Super P, Timcal) and polyvinyl difluoride (PVDF, Arkema) in ratios 75:20:5. N-methyl pyrrolidone (Aldrich,  $\geq 99.9\%$ ) was added in proportions 1 mL/100 mg of powder. One drop of the resulting slurry was spread on a titanium disk current collector (Ø11 mm, Goodfellow), and dried at 80 °C. The process was repeated until a satisfactory mass was achieved: 2 mg/cm<sup>2</sup> of active material for conventional electrochemical analysis and 10 mg/cm<sup>2</sup> in the case of *operando* XRD experiments. Disks of activated carbon (Kynol, ACC-509220) were used as counter electrodes in both three-electrode and coin cells, which were dried under vacuum at 70 °C overnight prior to use. The number of disks and their diameter (2–3, Ø11–12 mm) was adjusted to ensure large excess of capacity with respect to that of the working electrode. 0.5 M Mg(TFSI)<sub>2</sub> (Solvionic) in PC (Aldrich) was commonly used as electrolyte. Its water content was measured by Karl–Fisher titration and found to be < 20 ppm of H<sub>2</sub>O. The different electrolytes employed for setup optimization (section 2 Supporting Information) contained similar values of H<sub>2</sub>O.

3-electrode Swagelok cells<sup>[28]</sup> were assembled using Ag wire as quasi reference electrode in a setup described by Dugas et al.<sup>[29]</sup> All cells were assembled in a Ar glovebox with levels of H<sub>2</sub>O and O<sub>2</sub> lower than 0.5 ppm. Separators were made of cellulose filters (Prat Dumas, A007607), as classic borosilicate-based glass fiber (Whatman) resulted in sodium contamination (see details in section 2 Supporting Information). For the two step electrochemical protocol, the MnHCF electrodes were collected after pre-oxidation, washed with dimethyl carbonate (DMC), dried under vacuum, and placed in a new cell with fresh electrolyte. Cells were cycled at constant current equivalent to different C-rates, 1 C being equivalent to 1 mole of electrons (1 mol of K<sup>+</sup>, 0.5 mol of Mg<sup>2+</sup>) exchanged per formula unit.

## Computational Details

Spin polarized density functional theory calculations are performed using Vienna Ab-initio Simulation Package (VASP).<sup>[30,31]</sup> The exchange and correlation effects are approximated using Perdew–Burke–Ernzerhof parameterized generalized gradient approximation functional.<sup>[32]</sup> The core-valence interactions are defined using the projector augmented wave (PAW) method.<sup>[33]</sup> To account for the self-interaction error in the d-orbitals of transition metals, a +U correction of 3.9 eV is applied for Fe and Mn atoms. A plane-wave basis with an energy cut-off of 550 eV is used. The Brillouin zone is sampled using a k-point density of 4 Å<sup>-1</sup>. The convergence threshold is set to 10<sup>-6</sup> eV for the electronic density and 0.02 eV Å<sup>-1</sup> for the interatomic forces.

## Acknowledgements

The authors are grateful to Ashley Black (ICMAB-CSIC) and Jean-Frederic Martin (CEA) for helpful discussions and to François Fauth (ALBA synchrotron beamline scientist) for assistance during SXRD measurements (beamtime awarded under proposal 2021075225). ICMAB-CSIC authors are grateful to the Spanish Agencia Estatal de Investigación for Severo Ochoa FUNFUTURE (CEX2019-000917-S) distinction. Funding through the European Union's Horizon 2020 research and innovation programme under grant agreement No 824066 (E-MAGIC), Junta de Andalucía (EMERGIA\_00153, ProyExcel\_00330 PAIDI 2020), and project TED2021-129314A-100 funded by MCIN/AEI/10.13039/501100011033 and European Union NextGenerationEU/PRTR is gratefully acknowledged. Authors acknowledge support of the publication fee by the CSIC Open Access Publication Support Initiative through its Unit of Information Resources for Research (URICI).

## Conflict of Interests

The authors declare no conflict of interest.

## Data Availability Statement

The data that support the findings of this study are available from the corresponding author upon reasonable request.

**Keywords:** *magnesium batteries* • *Prussian blue analogues* • *operando XRD* • density functional theory

- [1] E. C. Evans, *Nature* **2015**, 526, 93–95.
- [2] B. Diouf, R. Pode, *Renew Energy* **2015**, 76, 375–380.
- [3] <https://www.nature.com/articles/d41586-021-01735-z>, *Nature* **2021**, 595, 7–7.
- [4] A. Ponrouch, J. Bitenc, R. Dominko, N. Lindahl, P. Johansson, M. R. Palacin, *Energy Storage Mater.* **2019**, 20, 253–262.
- [5] D. Aurbach, Z. Lu, A. Schechter, Y. Gofer, H. Gizbar, R. Turgeman, Y. Cohen, M. Moshkovich, E. Levi, *Nature* **2000**, 407, 724–727.



- [6] J. A. Blázquez, R. R. Maça, O. Leonet, E. Azaceta, A. Mukherjee, Z. Zhao-Karger, Z. Li, A. Kovalevsky, A. Fernández-Barquín, A. R. Mainar, P. Jankowski, L. Rademacher, S. Dey, S. E. Dutton, C. P. Grey, J. Drews, J. Häcker, T. Danner, A. Latz, D. Sotta, M. R. Palacin, J.-F. Martin, J. M. G. Lastra, M. Fichtner, S. Kundu, A. Kraytsberg, Y. Ein-Eli, M. Noked, D. Aurbach, *Energy Environ. Sci.* **2023**, *16*, 1964–1981.
- [7] F. Liu, T. Wang, X. Liu, L. Z. Fan, *Adv. Energy Mater.* **2021**, *11*, DOI 10.1002/aenm.202000787.
- [8] J. Muldoon, C. B. Bucur, T. Gregory, *Angew. Chem.* **2017**, *129*, 12232–12253.
- [9] I. D. Johnson, B. J. Ingram, J. Cabana, *ACS Energy Lett.* **2021**, *6*, 1892–1900.
- [10] M. Mao, T. Gao, S. Hou, C. Wang, *Chem. Soc. Rev.* **2018**, *47*, 8804–8841.
- [11] R. Trócoli, P. Parajuli, C. Frontera, A. P. Black, G. C. B. Alexander, I. Roy, M. E. Arroyo-De Dompablo, R. F. Klie, J. Cabana, M. R. Palacín, *ACS Appl. Energy Mater.* **2022**, *5*, 11964–11969.
- [12] B. Wang, Y. Han, X. Wang, N. Bahlawane, H. Pan, M. Yan, Y. Jiang, *iScience* **2018**, *3*, 110–133.
- [13] K. Hurlbutt, S. Wheeler, I. Capone, M. Pasta, *Joule* **2018**, *2*, 1950–1960.
- [14] J. Song, L. Wang, Y. Lu, J. Liu, B. Guo, P. Xiao, J. J. Lee, X. Q. Yang, G. Henkelman, J. B. Goodenough, *J. Am. Chem. Soc.* **2015**, *137*, 2658–2664.
- [15] R. Y. Wang, B. Shyam, K. H. Stone, J. N. Weker, M. Pasta, H. W. Lee, M. F. Toney, Y. Cui, *Adv. Energy Mater.* **2015**, *5*, DOI 10.1002/aenm.201401869.
- [16] R. Y. Wang, C. D. Wessells, R. A. Huggins, Y. Cui, *Nano Lett.* **2013**, *13*, 5748–5752.
- [17] A. I. Komayko, S. V. Ryazantsev, I. A. Trussov, N. A. Arkharova, D. E. Presnov, E. E. Levin, V. A. Nikitina, *ChemSusChem* **2021**, *14*, 1574–1585.
- [18] D. M. Kim, Y. Kim, D. Arumugam, S. W. Woo, Y. N. Jo, M. S. Park, Y. J. Kim, N. S. Choi, K. T. Lee, *ACS Appl. Mater. Interfaces* **2016**, *8*, 8554–8560.
- [19] A. L. Lipson, S. D. Han, S. Kim, B. Pan, N. Sa, C. Liao, T. T. Fister, A. K. Burrell, J. T. Vaughney, B. J. Ingram, *J. Power Sources* **2016**, *325*, 646–652.
- [20] M. S. Chae, J. Hyoung, M. Jang, H. Lee, S. T. Hong, *J. Power Sources* **2017**, *363*, 269–276.
- [21] Y. Tang, W. Li, P. Feng, M. Zhou, K. Wang, Y. Wang, K. Zaghbi, K. Jiang, *Adv. Funct. Mater.* **2020**, *30*, DOI 10.1002/adfm.201908754.
- [22] M. Fiore, S. Wheeler, K. Hurlbutt, I. Capone, J. Fawdon, R. Ruffo, M. Pasta, *Chem. Mater.* **2020**, *32*, 7653–7661.
- [23] X. Bie, K. Kubota, T. Hosaka, K. Chihara, S. Komaba, *J. Mater. Chem. A Mater* **2017**, *5*, 4325–4330.
- [24] X. Wu, C. Wu, C. Wei, L. Hu, J. Qian, Y. Cao, X. Ai, J. Wang, H. Yang, *ACS Appl. Mater. Interfaces* **2016**, *8*, 5393–5399.
- [25] F. Fauth, R. Boer, F. Gil-Ortiz, C. Popescu, O. Vallcorba, I. Peral, D. Fullà, J. Benach, J. Juanhuix, *Eur Phys J Plus* **2015**, *130*, DOI 10.1140/epjp/i2015-15160-y.
- [26] F. Fauth, I. Peral, C. Popescu, M. Knapp, *Powder Diff.* **2013**, *28*, S360–S370.
- [27] M. Herklotz, J. Weiß, E. Ahrens, M. Yavuz, L. Mereacre, N. Kiziltas-Yavuz, C. Dräger, H. Ehrenberg, J. Eckert, F. Fauth, L. Giebel, M. Knapp, *J. Appl. Crystallogr.* **2016**, *49*, 340–345.
- [28] D. Guyomard, J. M. Tarascon, *J. Electrochem. Soc.* **1992**, *139*, 937–948.
- [29] R. Dugas, J. D. Forero-Saboya, A. Ponrouch, *Chem. Mater.* **2019**, *31*, 8613–8628.
- [30] G. Kresse, J. Furthmüller, *Phys. Rev. B* **1996**, *16*, 11169–11186.
- [31] G. Kresse, J. Furthmüller, *Comput. Mater. Sci.* **1996**, *6*, 15–50.
- [32] J. P. Perdew, K. Burke, M. Ernzerhof, *Phys. Rev. Lett.* **1996**, *78*, 3865–3868.
- [33] P. E. Blochl, *Phys. Rev. Lett.* **1994**, *50*, 17953–17979.

Manuscript received: August 18, 2023

Revised manuscript received: October 30, 2023

Accepted manuscript online: November 2, 2023

Version of record online: November 30, 2023